

Spectral mapping of thermal conductivity through nanoscale ballistic transport

Yongjie Hu^{1,2}, Lingping Zeng¹, Austin J. Minnich³, Mildred S. Dresselhaus⁴ and Gang Chen^{1*}

Controlling thermal properties is central to many applications, such as thermoelectric energy conversion and the thermal management of integrated circuits. Progress has been made over the past decade by structuring materials at different length scales, but a clear relationship between structure size and thermal properties remains to be established. The main challenge comes from the unknown intrinsic spectral distribution of energy among heat carriers. Here, we experimentally measure this spectral distribution by probing quasi-ballistic transport near nanostructured heaters down to 30 nm using ultrafast optical spectroscopy. Our approach allows us to quantify up to 95% of the total spectral contribution to thermal conductivity from all phonon modes. The measurement agrees well with multiscale and first-principles-based simulations. We further demonstrate the direct construction of mean free path distributions. Our results provide a new fundamental understanding of thermal transport and will enable materials design in a rational way to achieve high performance.

Designing structures at the nanoscale to control their physical properties has shown great promise in driving materials to high performance well beyond the state of the art^{1–16}. In particular, different nanostructuring approaches have recently been extended to manipulate thermal properties for energy conversion, thermal management and novel thermal insulation^{5–14,17,19}. Rational ways to control thermal conductivity are strongly desired but remain challenging, because thermal transport generally involves a spectral distribution of heat carriers and this distribution is unknown in most solids. In most semiconductors and dielectrics, these heat carriers are primarily lattice vibrations, or phonons²⁰. Macroscopic thermal conductivity is the sum of the contributions from all phonon modes²¹, which span a wide spectrum in the Brillouin zone. Quantifying the contributions of different phonon modes to the thermal conductivity is critical for using nanostructuring approaches to tailor the thermal conductivity, but this information remains elusive for most materials. At present, most materials are designed by a trial-and-error process¹³. Extensive theoretical work, particularly that using first-principles density functional theory (DFT) calculations, has shown progress in predicting the spectral distribution, but is limited by computational costs^{10,22–25}. Experimentally, inelastic neutron scattering is a classical technique that provides a powerful tool to study phonon spectra and lifetimes^{26,27}, but this approach is limited to the characterization of single-crystal materials and requires facilities that are not widely available. In this Article we demonstrate a desk-top approach to experimentally determine and construct the full spectral distribution of the thermal conductivity of a variety of materials by utilizing observations of quasi-ballistic thermal transport.

Thermal spectra and quasi-ballistic transport

The key metric to quantify the spectral distribution is the cumulative thermal conductivity, $\Phi(\Lambda_m) = \int_0^{\Lambda_m} (1/3)C \cdot v \cdot \Lambda(d\Lambda/d\omega)^{-1} d\Lambda$ (for isotropic media), where C , v and Λ are the mode-dependent heat capacity, group velocity and phonon mean free path (MFP)^{21,28},

respectively. MFPs are the characteristic lengths that describe the distance the heat carriers can transmit thermal energy before being scattered, and can span several orders of magnitude, for example, from ~ 1 nm to ~ 1 mm. The cumulative thermal conductivity, $\Phi(\Lambda_m)$, represents the contribution to the total thermal conductivity from all phonons with MFPs less than a certain value, Λ_m . This quantification projects the spectral contributions of the thermal conductivity into characteristic length scales, and is useful for the direct prediction of thermal transport in more complex nanostructured materials²¹. In fact, reducing the phonon thermal conductivity by using nanostructures with characteristic dimensions smaller than their bulk MFPs has become a powerful approach in thermoelectric energy conversion^{3,5,6,8,12,13,18,29}. The rational design of material structures, which has great potential to improve thermal device performance in the future, relies on this quantitative spectral information. The goal of this work is to quantify the thermal spectra in different materials based on two essential steps: measuring the size-dependent ballistic transport across the full range of phonon MFPs and the successful conversion of direct measurements into intrinsic MFP distributions.

Our approach to measuring a wide range of size-dependent ballistic transport is based on exploiting quasi-ballistic heat conduction around nanostructured heat sources. The basic physical picture is illustrated in Fig. 1a. In the measurement, hot phonons travel from the heater into the underlying substrate material. The heat transfer regime is controlled by a characteristic thermal length, which is proportional to the heater size D , compared to phonon MFPs. In the diffusive limit, when $D \gg \Lambda$, propagating phonons experience enough scattering to reach local thermal equilibrium. In this case, Fourier's law accurately describes the transport and the thermal conductivity of materials is simply the bulk value (k_{bulk}). From kinetic theory²⁰, the contribution to the total thermal conductivity from a specific phonon mode is $k_{\omega,\text{bulk}} = (1/3)C_{\omega} \cdot v_{\omega} \cdot \Lambda_{\omega}$. As the heater size D is reduced, those phonons with $D < \Lambda$ will have few opportunities to scatter. In the ballistic limit ($D \ll \Lambda$), phonons propagate analogously to thermal radiation over the

¹Department of Mechanical Engineering, Massachusetts Institute of Technology, Cambridge, Massachusetts 02139, USA. ²Department of Mechanical and Aerospace Engineering, University of California, Los Angeles, California 90095, USA. ³Division of Engineering and Applied Science, California Institute of Technology, Pasadena, California 91125, USA. ⁴Department of Electrical Engineering and Department of Physics, Massachusetts Institute of Technology, Cambridge, Massachusetts 02139, USA. *e-mail: gchen2@mit.edu

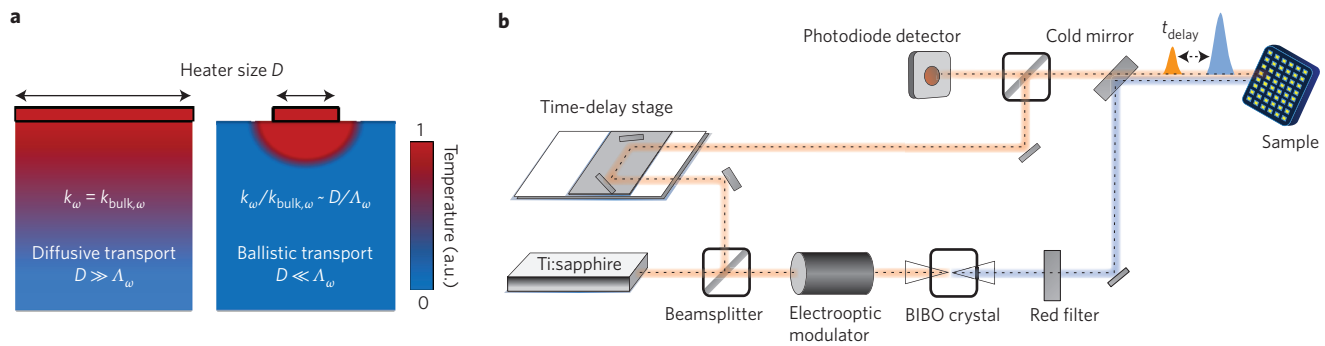


Figure 1 | Ultrafast optical spectroscopy and size-dependent thermal transport. **a**, Illustration of thermal transport, affected by heater size D and suppression of the effective thermal conductivity (k_ω) for individual phonon modes in the diffusive region (left, $D \gg \Lambda_\omega$) and in the ballistic region (right, $D \ll \Lambda_\omega$). **b**, Schematic of the time-domain thermoreflectance measurement set-up. Blue and orange routes represent pump and probe laser beams, respectively.

whole region with a characteristic length $\sim D$. Importantly, the heat flux in the ballistic regime is very different from that in the diffusive regime, and these deviations provide information about the MFPs of thermal phonons. The ratio of the ballistic to the diffusive heat flux reveals that the contribution of each ballistic phonon mode to the total thermal conductivity will be suppressed compared to the Fourier law prediction as $k_\omega/k_{\text{bulk},\omega} \sim D/\Lambda_\omega$ (ref. 30), although the exact relationship depends on geometry, which will be discussed in more detail later in this Article. The deviation from the Fourier law was observed at a low temperature, when some phonons can have very long MFPs, using heating and electrical-resistance thermometry along a small doped region in a suspended silicon membrane based on local temperature measurement^{19,31}. Some of the co-authors observed this phenomenon by measuring the thermal conductivity of silicon using laser heating with different beam diameters, and suggested this as a tool to study phonon MFPs³². However, the laser beam diameter was greater than 10 μm , and experimental observation was again limited to very low temperatures when the MFPs are much longer. Due to the optical diffraction limit, it is not clear how this approach can be extended below 1 μm , making it difficult to apply to most materials for which a large portion of phonons have MFPs of hundreds of nanometres. Other approaches are also being pursued to study phonon MFPs but with limitations. Frequency-domain modulation was used to define the thermal diffusion length^{33,34}, but this technique was limited to materials with low thermal conductivity. Grating techniques^{35,36} probing the differences between the peaks and valleys of the temperature profile are limited by the laser wavelength or require materials to be optically transparent. At present, there is no measurement capable of covering a wide range of phonon MFPs—from nanometres to tens of micrometres—in most materials. More importantly, all of these experiments have oversimplified the interpretation of size-dependent transport by assuming that phonons with MFPs larger than the characteristic size do not contribute to heat conduction. Therefore, a clear experimental approach to measure the intrinsic phonon MFP spectra with a rigorous interpretation is critically important and needs to be developed. Here, we demonstrate a generic approach that can be applied to many materials, which for the first time measures contributions of up to $\sim 95\%$ of the total thermal conductivity from all phonon modes. The measurement strategy presented here systematically varies the heater size D down to 30 nm through a hybrid nanostructure design, thus resulting in a gradual suppression of the phonon modes due to ballistic transport. By measuring the reduction in the thermal conductivity, we can obtain the contribution to the thermal conductivity from phonon modes with $\Lambda \sim D$. Furthermore, we demonstrate the successful conversion

of the observed ballistic phonon transport at different sizes to map the intrinsic phonon MFP distribution, which will be described in detail later in this Article.

Transient and size-dependent measurements

In the present experiments, the thermal conductivity was measured using a time-domain thermoreflectance (TDTR) technique³⁷, as shown in Fig. 1b (see Methods). A femtosecond laser pulse is split into a pump and a probe pulse. The pump pulse heats the sample surface and the probe pulse samples the change in reflectance of a metal transducer film with a delay time controlled by a mechanical delay line. The optical reflectance change can be linearly related to the surface temperature change of the sample with sub-picosecond temporal resolution: $\Delta R \propto C_{\text{TR}} \Delta T$, where C_{TR} is the material-dependent thermoreflectance coefficient. From the measured surface temperature decay, the effective thermal conductivity (k_{eff}) of the sample materials can be obtained by fitting to a multilayer model derived from Fourier's law^{37,38}.

There are two major challenges in expanding the technique to cover the wide range of length scales spanned by phonon MFPs. The first is how to generate nanoscale heat sources and the second is to avoid electron-hole generation in the substrate, as this process complicates the analysis of thermoreflectance signals. To overcome the first challenge we used nanoscale metallic patterns with variable size on the sample surface to control the characteristic length for thermal transport. As shown in Fig. 2a, a metallic pattern of variable size D (30 nm to 60 μm) served as the effective heater after absorbing the pump light, rather than the optical beam itself. To avoid electron-hole generation by the underlying substrate material, a hybrid bilayer structure was used to localize the heating source and minimize contributions to the reflected probe pulse from the surrounding regions (see Methods). This hybrid structure uses a polymer layer and two different metals to ensure that the detected thermal reflectance change signal represents heat transfer through the substrate.

The hybrid structure is effective for two reasons. First, due to the periodically modulated heat flux input from the pump pulse, the temperature profile decays exponentially with a characteristic length equal to the thermal penetration depth L_p . In the polymer layer, the thermal penetration depth is very small due to its low thermal diffusivity α . A polymer layer thicker than $L_p \approx 100$ nm ensures that the periodic heating will not affect the underlying sample materials under the experimental conditions. Thus, the temperature rise of the metal in direct contact with the substrate is not affected by heating of the metal on top of the polymer. Second, a metal with a small thermoreflectance change (ΔR) is used on the polymer. The metal in direct contact with the sample

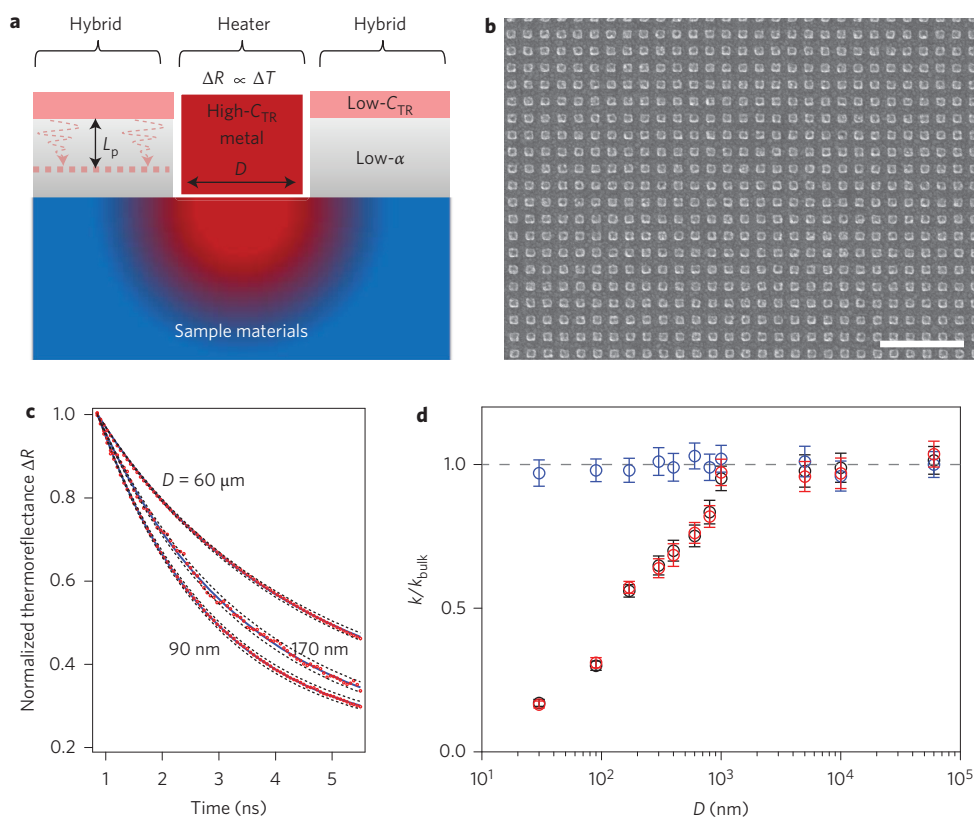


Figure 2 | Size-dependent heating using hybrid nanostructures and thermoreflectance measurements. **a**, Schematic of hybrid structures for local heating and temperature detection. The sample material is heated up locally by the heater and its surface temperature change (ΔT) is detected as the thermoreflectance signal (ΔR). **b**, SEM image of a typical sample. Aluminium patterns in a regular array on the sample serve as effective heaters, and the laterally separated surrounding dark region contains hybrid structures consisting of a low-thermoreflectance top layer of metal and a low-thermal-diffusivity bottom layer of polymer. Scale bar, 1 μm . **c**, Normalized thermoreflectance change ΔR versus time, fit by the diffusive model. Experimental curves (red circles) and fits from the multilayer thermal transport model (blue lines) for $D = 60 \mu\text{m}$, 170 nm and 90 nm. Calculated curves (black dots) using the thermal conductivity changed by $\pm 10\%$ of best values are plotted to illustrate the measurement sensitivity. **d**, Experimental results for the size-dependent effective thermal conductivity normalized to the bulk value for a validation measurement. Amorphous SiO_2 (blue circles) shows no obvious size-dependent effective thermal conductivity. Metallic pattern arrays (red circles) and a hybrid design (black circles) show similar results for sapphire. Error bars indicate the standard deviations in data fitting.

materials has a large thermoreflectance change such that the measured signal is mainly contributed by heating the substrate. Figure 2b presents a scanning electron microscopy (SEM) image of a regular array of such patterns over a large area.

As a proof-of-concept example to validate the accuracy of our thermal analysis model and the confinement efficiency of the hybrid design, the thermal conductivity was first measured with different heater sizes for glass and sapphire. Figure 2c shows typical experimental data for different heater sizes D . The measured thermoreflectance signal $\Delta R(t)$ represents the surface temperature decay of the heater, $\Delta R(t) \propto \Delta T(t)$ and strongly depends on the thermal properties of the underlying materials. Therefore, by fitting the time-dependent curve with a multilayer diffusive model, the effective thermal conductivity k can be obtained (results are shown in Fig. 2d in terms of k/k_{bulk}). The thermal conductivity of glass was measured as $1.4 \text{ W m}^{-1} \text{ K}^{-1}$, consistent with the literature, showing no obvious size dependence. Note that the measured k is the effective thermal conductivity predicted using a diffusive transport model (for example, one based on Fourier's law), and this k value will be smaller than the actual value if ballistic transport occurs ($\text{MFP} > D$). For disordered oxides, such as glasses, the atoms oscillate with random phases and there are no collective lattice motions, meaning ballistic transport does not occur over the length scales probed in our experiment. Although recent calculations³⁹ suggest that propagating phonon modes with long MFPs make a considerable contribution to the

thermal conductivity of amorphous SiO_2 , our results do not show appreciable size-dependent thermal conductivity in glass and are consistent with ref. 34. Second, we performed a measurement on sapphire with a pure metallic pattern and the hybrid design. Sapphire is transparent to the optical wavelength used in the measurement, so, even without the hybrid structure, there is a clearly defined local heating area. The good agreement between the two results confirms that the hybrid design and modelling can provide efficient local heating and surface temperature detection. Finally, unlike glass, the thermal conductivity of sapphire starts to drop off when D is reduced below $1 \mu\text{m}$. We attribute the change in effective thermal conductivity to size-dependent ballistic thermal transport, and the result indicates that most phonons in sapphire have MFPs $< 1 \mu\text{m}$. To obtain a more detailed understanding of the intrinsic phonon spectral distribution from the heater size-dependent thermal conductivity, we next apply this approach to silicon, using silicon as a model system material.

Multiscale and first-principles simulations

The thermal properties of silicon have been studied extensively, especially using first-principles DFT calculations²³. However, experimental measurements are limited to long MFP phonons^{32,34,35}. We measured the normalized effective thermal conductivities of Si (k/k_{bulk}) as shown in Fig. 3a. When the heater size is large ($D = 60 \mu\text{m}$, as in the film case), the measured thermal conductivity approaches the literature value for bulk silicon ($k = 142 \text{ W m}^{-1} \text{ K}^{-1}$).

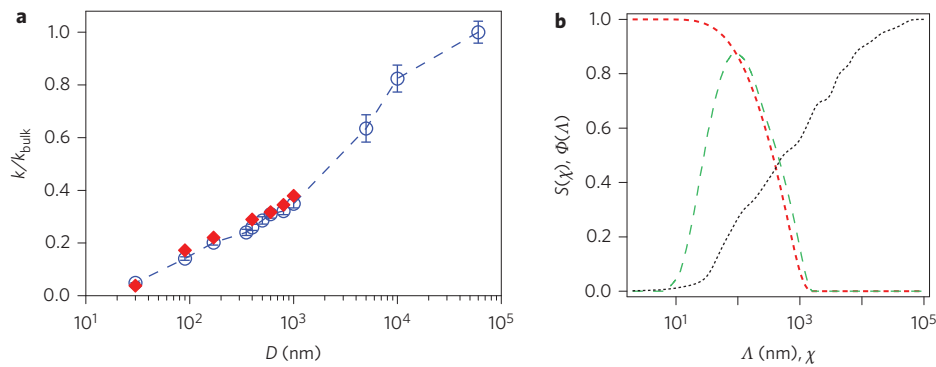


Figure 3 | Size-dependent effective thermal conductivity k/k_{bulk} of silicon and phonon mode suppression. **a, Normalized experimental data (blue circles) and Monte Carlo simulation (red diamonds) for silicon. Error bars indicate the standard deviations in data fitting. **b**, Normalized MFP distribution $\Phi(\Lambda)$ of silicon calculated by DFT (black dotted line), the suppression factor $S(\chi)$ calculated for $D = 1 \mu\text{m}$ (red dashed line) and its differential curve as the computation kernel function $K(\chi)$ (green dashed line).**

When D is reduced to ~ 30 nm, more than 90% of the total thermal conductivity is suppressed. As a comparison, classical kinetic theory²⁰ estimates the thermal conductivity as $k = (1/3)C \cdot v \cdot \bar{\Lambda}$, where the averaged MFP for silicon is $\bar{\Lambda} = 41$ nm, by using the volumetric heat capacity C and the branch-averaged sound velocity v_s . This grey approximation severely underestimates the contribution from phonons with long MFPs, due to an overestimated weighted group velocity of acoustic phonons at room temperature and optical phonon contributions to k (refs 31, 40). This result emphasizes the necessity of using a spectral distribution for an accurate description of thermal transport.

To better understand and validate the accuracy of our thermal measurement, we performed simulations based on first-principles calculations to predict the effective thermal conductivity of silicon for the three-dimensional heating geometry in the measurement. We used a recently developed variance-reduced stochastic Monte Carlo method⁴¹ to solve the three-dimensional spectral-dependent phonon Boltzmann transport equation, with phonon lifetimes calculated from first-principles DFT and full phonon dispersion relations²³. The computed surface temperature is fit with a diffusive solution to obtain the effective thermal conductivity. The numerically predicted data plotted in Fig. 3a show good agreement with the experimental data. We also varied the interface thermal conductance values in our simulation by changing the phonon transmittance, and we found that they have little influence on the simulated effective thermal conductivity (Supplementary Section 2.5). These results demonstrate that our approach can precisely capture the physics of ballistic transport and the spectral contributions from all phonon modes, although it is understood that the presented technique may not be suitable for all transducing metal–substrate combinations due to the mismatch in the phonon spectra and crystallography, such as occurs in highly anisotropic materials.

Reconstruction of the spectral distribution

A further important step is to quantitatively reconstruct the intrinsic spectral distribution from the size-dependent measurements. In earlier studies, the geometric size was often directly equated to the phonon MFP, and phonons with MFPs larger than this size were assumed not to contribute to the measured thermal conductivity. In fact, size dependence is heavily dependent on the experimental device geometry, numerically expressed as a suppression function S , whereas the MFP is an intrinsic characteristic of materials^{21,42–45}. Previous works did not use a reconstruction technique to connect characteristic sizes to the MFP, explaining why the size-dependent thermal conductivity values in the literature do not agree with one another for the same materials (that is, silicon)^{31–35}. Numerically, the measurements are linked to the desired MFP distribution by a

suppression function S that describes the reduction in heat flux carried by ballistic phonons compared to the Fourier law prediction^{21,42,43}. S is a geometric factor and is only determined by the specific heating geometry. In the present experimental configuration, S is a function depending on both the heater width D and the inter-heater spacing L (ref. 46) via two non-dimensional parameters, Λ/D and D/L . Our fabricated structure maintains D/L as a constant, so S depends only on Λ/D . Mathematically, the size-dependent effective thermal conductivity $k(D)$ is related to the differential spectral distribution $\phi(\Lambda)$ by

$$k(D) = \int_0^\infty S(\chi) \cdot \phi(\Lambda) d\Lambda = \int_0^\infty K(\chi) \cdot \Phi(\Lambda) d\Lambda \quad (1)$$

where $\chi = \Lambda/D$, the cumulative distribution $\Phi(\Lambda) = \int_0^\Lambda \phi(\Lambda) d\Lambda$ and the computational kernel $K(\chi) = -dS/d\chi$. However, the suppression function $S(\chi)$ is only available for the simplest case in one dimension^{21,42,43}, and $S(\chi)$ is difficult to calculate here due to the three-dimensional geometric complexity. To solve this issue we developed the suppression function for complex three-dimensional heating structures using a benchmark approach: by leveraging the full spectrum of the experimentally measured size-dependent data and the MFP distribution from DFT calculations, $S(\chi)$ can be obtained by using the silicon data as the benchmark reference (see Methods). The calculated $S(\chi)$ and kernel function $K(\chi)$ (after normalization) (scaled by a factor of 2) for $D = 1 \mu\text{m}$ are plotted in Fig. 3b.

Note that a recent work has reported that Fourier's law fails for anisotropic materials and that the interface can play a role in ballistic transport⁴⁷. Our calibration approach to determine the suppression function automatically takes these effects into account and is supported by previous simulations⁴⁵. Furthermore, the suppression function is approximately independent of the material under consideration and can thus be used to study other materials^{21,42–45}. We demonstrate this ability by directly reconstructing the spectral distribution of the thermal conductivity from measurements on several materials. Impurity doping and alloying are common methods used in thermoelectric materials development to effectively reduce a material's thermal conductivity while improving the electrical conductivity, yet precisely which phonons are scattered by these defects remains unclear. To obtain insight into this scattering mechanism, we measured the size-dependent thermal conductivity for a SiGe alloy (Fig. 4a). Again, phonon modes contributing over 90% of the total thermal conductivity can be accounted for by reducing the heater size from $\sim 100 \mu\text{m}$ to 30 nm. Using the suppression function $S(\chi)$, we reconstructed the spectral distribution of the thermal conductivity for $\text{Si}_{0.992}\text{Ge}_{0.008}$ (indicated by green circles in Fig. 4b).

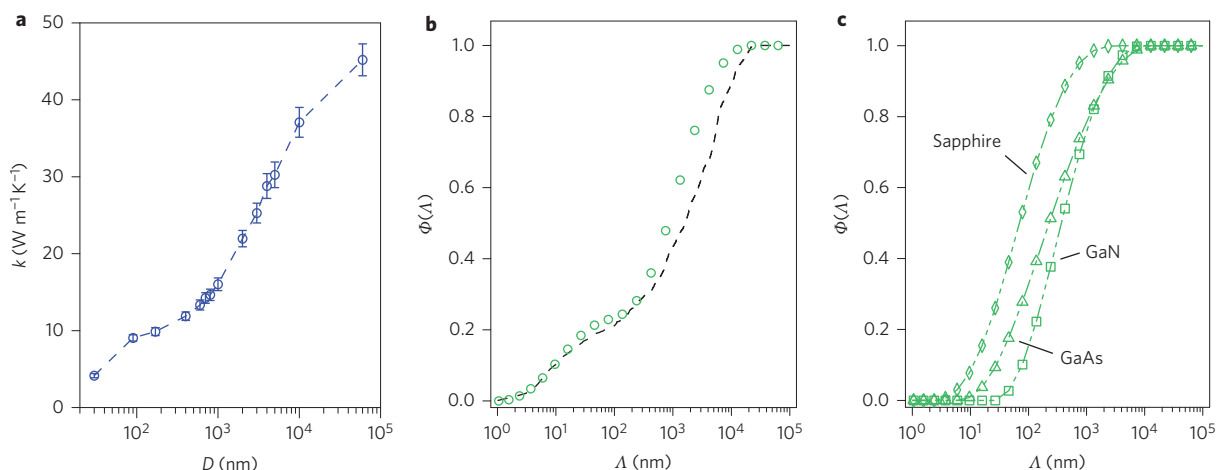


Figure 4 | Reconstruction of the spectral distribution of the thermal conductivity. **a**, Size-dependent effective thermal conductivity of $\text{Si}_{0.992}\text{Ge}_{0.008}$. Error bars indicate the standard deviations in data fitting. **b**, Comparison of the reconstructed phonon MFP distribution of $\text{Si}_{0.992}\text{Ge}_{0.008}$ (green circles) and the DFT calculation (black dashed line). **c**, Reconstructed phonon MFP distributions for sapphire, GaAs and GaN.

Comparison of experiment and DFT calculation

To verify the reliability of the phonon spectra thus constructed, we compared them with DFT calculations for the same material using a previously published method^{22–24}. The phonon spectra from the experiments and from DFT calculations indeed show good agreement with each other (Fig. 4b). Notably, the SiGe data capture an interesting phenomenon: the MFP distribution curve exhibits two regimes due to different phonon scattering mechanisms. The first is a large-slope regime (of the semi-log plot) in the long MFP range ($>1\ \mu\text{m}$), which is similar to the crystalline silicon MFP distribution, where anharmonic phonon scattering is dominant. A regime with a smaller slope is observed for the short MFP range ($<1\ \mu\text{m}$) and can be attributed to impurity scattering from Ge atoms. The MFP distribution shows that even with only 0.8% of Ge atoms, random Ge impurity atoms can effectively scatter phonons with MFPs up to $1\ \mu\text{m}$ and reduce the bulk thermal conductivity from $142\ \text{W m}^{-1}\ \text{K}^{-1}$ (in silicon) to $46\ \text{W m}^{-1}\ \text{K}^{-1}$.

The approach developed here can be used to measure the spectral distribution of the thermal conductivity in different materials. Figure 4c presents the reconstructed MFP distribution for sapphire, GaN (wurtzite) and GaAs. The measured thermal spectra are unique and can vary greatly for different materials. The significance of our work is twofold. First, the measured spectral distribution provides essential information for phonon engineering, especially in the design of thermoelectric materials to achieve low thermal conductivity. Second, the spectral distribution can provide important information for the thermal management of ultra-small semiconductor electronic devices. Thermal management has become a well-known limiting factor in the performance of microelectronics. Although size effects on the thermal conductivity of thin films and nanowires are well known now due to phonon scattering at boundaries^{48,49}, our work shows that heat spreading to large substrates is also limited by size effects arising from ballistic heat transport away from the heat generation region. For example, from our results, the thermal conductivity of Si and GaN can be reduced to about 10% of the bulk value when the heater size is less than 50 nm and 100 nm, respectively. In semiconductor devices such as metal-oxide-semiconductor field-effect transistor (MOSFETs), most heat is typically dissipated in the drain region of the device, which is on the order of tens of nanometres¹⁷, and our results show that the temperature rise in these regions may be higher than predictions based on the bulk thermal conductivity. When devices are manufactured at different length scales, knowledge of

these spectral contributions can provide a more accurate evaluation of their capability to exchange heat from hot spots to the environment as well as for local temperature-dependent electrical transport¹⁷. In the Supplementary Information, we also give an approximate expression for the effective thermal conductivity so that size effects can be estimated quickly.

Conclusion

In summary, we have directly measured the phonon spectral contributions to thermal conductivity based on the quasi-ballistic transport that occurs near nanoscale heat sources. We have demonstrated that the experimental results for the MFP distributions in a SiGe alloy sample agree well with first-principles-based simulations, and we can apply the method to several other materials including GaAs, GaN and sapphire. Our experimental approach provides a general route to experimentally quantify contributions to heat transport from phonons with different MFPs across the entire phonon spectrum. The measured results can be directly applied to better design thermal properties using nanostructured materials for energy applications. The results also have significant implications for the thermal management of ultra-small electronic devices¹⁷. We expect that future work using similar methods combined with theoretical calculations will lead to a clearer microscopic description of thermal transport in nanostructures and will open up new opportunities to improve material performance through the optimal control of energy carriers.

Methods

Methods and any associated references are available in the [online version of the paper](#).

Received 5 April 2014; accepted 23 April 2015;
published online 1 June 2015

References

1. Chu, S. & Majumdar, A. Opportunities and challenges for a sustainable energy future. *Nature* **488**, 294–303 (2012).
2. *Quadrennial Technology Review* (US Department of Energy, 2011); available at <http://energy.gov/qr>
3. Majumdar, A. Materials science. Thermoelectricity in semiconductor nanostructures. *Science* **303**, 777–778 (2004).
4. Bell, L. E. Cooling, heating, generating power, and recovering waste heat with thermoelectric systems. *Science* **321**, 1457–1461 (2008).
5. Poudel, B. *et al.* High-thermoelectric performance of nanostructured bismuth antimony telluride bulk alloys. *Science* **320**, 634–638 (2008).
6. Biswas, K. *et al.* High-performance bulk thermoelectrics with all-scale hierarchical architectures. *Nature* **489**, 414–418 (2012).

7. Lee, W. *et al.* Heat dissipation in atomic-scale junctions. *Nature* **498**, 209–212 (2013).
8. Boukai, A. I. *et al.* Silicon nanowires as efficient thermoelectric materials. *Nature* **451**, 168–171 (2008).
9. Seol, J. H. *et al.* Two-dimensional phonon transport in supported graphene. *Science* **328**, 213–216 (2010).
10. Luckyanova, M. N. *et al.* Coherent phonon heat conduction in superlattices. *Science* **338**, 936–939 (2012).
11. Dames, C. Thermal materials: pulling together to control heat flow. *Nature Nanotech.* **7**, 82–83 (2012).
12. Singh, D. J. Nanostructuring and more. *Nature Mater.* **7**, 616–617 (2008).
13. Dresselhaus, M. S. *et al.* New directions for low-dimensional thermoelectric materials. *Adv. Mater.* **19**, 1043–1053 (2007).
14. Kraemer, D. *et al.* High-performance flat-panel solar thermoelectric generators with high thermal concentration. *Nature Mater.* **10**, 532–538 (2011).
15. Yan, H. *et al.* Programmable nanowire circuits for nanoprocessors. *Nature* **470**, 240–244 (2011).
16. Yin, X., Ye, Z., Rho, J., Wang, Y. & Zhang, X. Photonic spin Hall effect at metasurfaces. *Science* **339**, 1405–1407 (2013).
17. Pop, E., Sinha, S. & Goodson, K. E. Heat generation and transport in nanometer-scale transistors. *Proc. IEEE* **94**, 1587–1601 (2006).
18. Heremans, J. P., Dresselhaus, M. S., Bell, L. E. & Morelli, D. T. When thermoelectrics reached the nanoscale. *Nature Nanotech.* **8**, 471–473 (2013).
19. Marconnet, A. M., Panzer, M. A. & Goodson, K. E. Thermal conduction phenomena in carbon nanotubes and related nanostructured materials. *Rev. Mod. Phys.* **85**, 1295–1326 (2013).
20. Ziman, J. M. *Electrons and Phonons: The Theory of Transport Phenomena in Solids* (Oxford Classic Texts in the Physical Sciences, 1960).
21. Yang, F. & Dames, C. Mean free path spectra as a tool to understand thermal conductivity in bulk and nanostructures. *Phys. Rev. B* **87**, 035437 (2013).
22. Broido, D. A., Malorny, M., Birner, G., Mingo, N. & Stewart, D. A. Intrinsic lattice thermal conductivity of semiconductors from first principles. *Appl. Phys. Lett.* **91**, 231922 (2007).
23. Esfarjani, K., Chen, G. & Stokes, H. T. Heat transport in silicon from first-principles calculations. *Phys. Rev. B* **84**, 085204 (2011).
24. Garg, J., Bonini, N., Kozinsky, B. & Marzari, N. Role of disorder and anharmonicity in the thermal conductivity of silicon–germanium alloys: a first-principles study. *Phys. Rev. Lett.* **106**, 045901 (2011).
25. Lindsay, L., Broido, D. A. & Reinecke, T. L. First-principles determination of ultrahigh thermal conductivity of boron arsenide: a competitor for diamond? *Phys. Rev. Lett.* **111**, 025901 (2013).
26. Delaire, O. *et al.* Giant anharmonic phonon scattering in PbTe. *Nature Mater.* **10**, 614–619 (2011).
27. Ma, J. *et al.* Glass-like phonon scattering from a spontaneous nanostructure in AgSbTe₂. *Nature Nanotech.* **8**, 445–451 (2013).
28. Dames, C. & Chen, G. *Thermoelectrics Handbook, Macro to Nano* (ed. Rowe, D. M.) Ch. 42 (CRC Press, 2006).
29. Hochbaum, A. I. *et al.* Enhanced thermoelectric performance of rough silicon nanowires. *Nature* **451**, 163–167 (2008).
30. Chen, G. Nonlocal and nonequilibrium heat conduction in the vicinity of nanoparticles. *J. Heat Transfer* **118**, 539–545 (1996).
31. Sverdrup, P. G., Sinha, S., Asheghi, M., Uma, S. & Goodson, K. E. Measurement of ballistic phonon conduction near hotspots in silicon. *Appl. Phys. Lett.* **78**, 3331 (2001).
32. Minnich, A. J. *et al.* Thermal conductivity spectroscopy technique to measure phonon mean free paths. *Phys. Rev. Lett.* **107**, 095901 (2011).
33. Koh, Y. & Cahill, D. Frequency dependence of the thermal conductivity of semiconductor alloys. *Phys. Rev. B* **76**, 075207 (2007).
34. Regner, K. T., Majumdar, S. & Malen, J. A. Instrumentation of broadband frequency domain thermoreflectance for measuring thermal conductivity accumulation functions. *Rev. Sci. Instrum.* **84**, 064901 (2013).
35. Johnson, J. A. *et al.* Direct measurement of room-temperature nondiffusive thermal transport over micron distances in a silicon membrane. *Phys. Rev. Lett.* **110**, 025901 (2013).
36. Siemens, M. E. *et al.* Quasi-ballistic thermal transport from nanoscale interfaces observed using ultrafast coherent soft X-ray beams. *Nature Mater.* **9**, 26–30 (2009).
37. Schmidt, A. J., Chen, X. & Chen, G. Pulse accumulation, radial heat conduction, and anisotropic thermal conductivity in pump–probe transient thermoreflectance. *Rev. Sci. Instrum.* **79**, 114902 (2008).
38. Cahill, D. G. Analysis of heat flow in layered structures for time-domain thermoreflectance. *Rev. Sci. Instrum.* **75**, 5119 (2004).
39. He, Y., Donadio, D. & Galli, G. Heat transport in amorphous silicon: interplay between morphology and disorder. *Appl. Phys. Lett.* **98**, 144101 (2011).
40. Chen, G. Thermal conductivity and ballistic-phonon transport in the cross-plane direction of superlattices. *Phys. Rev. B* **57**, 14958–14973 (1998).
41. Péraud, J.-P. M. & Hadjiconstantinou, N. G. Efficient simulation of multidimensional phonon transport using energy-based variance-reduced Monte Carlo formulations. *Phys. Rev. B* **84**, 205331 (2011).
42. Maznev, A. A., Johnson, J. A. & Nelson, K. A. Onset of nondiffusive phonon transport in transient thermal grating decay. *Phys. Rev. B* **84**, 195206 (2011).
43. Minnich, A. J. Determining phonon mean free paths from observations of quasiballistic thermal transport. *Phys. Rev. Lett.* **109**, 205901 (2012).
44. Collins, K. C. *et al.* Non-diffusive relaxation of a transient thermal grating analyzed with the Boltzmann transport equation. *J. Appl. Phys.* **114**, 104302 (2013).
45. Ding, D., Chen, X. & Minnich, A. J. Radial quasiballistic transport in time-domain thermoreflectance studied using Monte Carlo simulations. *Appl. Phys. Lett.* **104**, 143104 (2014).
46. Zeng, L. & Chen, G. Disparate quasiballistic heat conduction regimes from periodic heat sources on a substrate. *J. Appl. Phys.* **116**, 064307 (2014).
47. Wilson, R. B. & Cahill, D. G. Anisotropic failure of Fourier theory in time-domain thermoreflectance experiments. *Nature Commun.* **5**, 5075 (2014).
48. Goodson, K. E. & Ju, Y. S. Heat conduction in novel electronic films. *Annu. Rev. Mater. Sci.* **29**, 261–293 (1999).
49. Cahill, D. G. *et al.* Nanoscale thermal transport. II. 2003–2012. *Appl. Phys. Rev.* **1**, 011305 (2014).

Acknowledgements

The authors thank J. Garg for providing DFT data on Si_{0.992}Ge_{0.008}, and D. Broido, N.G. Hadjiconstantinou, A. Marconnet, J.K. Tong, J.-P. Péraud, W. Dai, A. Maznev, K. Nelson, J. Cuffe, M. Luckyanova and K. Collins for discussions. This material is based on work supported as part of the ‘Solid State Solar-Thermal Energy Conversion Center (S3TEC)’, an Energy Frontier Research Center funded by the US Department of Energy, Office of Science, Office of Basic Energy Sciences (grant no. DE-SC0001299/DE-FG02-09ER46577). Y.H. is partially supported by the Battelle/MIT Fellowship.

Author contributions

Y.H. and G.C. developed the concept. Y.H. prepared the samples and performed the experiments. L.Z. performed the Monte Carlo simulation. Y.H. performed the numerical calculations on convex optimizations. All authors discussed the results and commented on the manuscript. G.C. directed the research.

Additional information

Supplementary information is available in the [online version](#) of the paper. Reprints and permissions information is available online at www.nature.com/reprints. Correspondence and requests for materials should be addressed to G.C.

Competing financial interests

The authors declare no competing financial interests.

Methods

Experimental details. Thermal transport was characterized using the TDTR technique³⁷. The basic set-up is presented in Fig. 1b. A tunable Ti:sapphire laser emits a train of 200 fs pulses at a repetition rate of 80.7 MHz and a central wavelength of 800 nm. The light is divided into pump and probe beams by the first beamsplitter, with a large power ratio between the two beams. The pump beam provides the thermal excitation and the probe beam serves as a non-invasive temperature sensor by measuring the change in reflectance due to the temperature change. The pump beam (with spot size of 60 μm) passes through an electro-optic modulator with a sine-wave modulation up to 20 MHz and then through a bismuth triborate (BIBO) crystal, where its frequency is doubled to 400 nm. The probe beam (with spot size of 10 μm) is controlled with a delay time t_{delay} (up to 6 ns) by a time-delay stage, and its reflected intensity is measured by a photodiode detector (Thorlabs PDA36A).

Sample preparation. Metallic patterns and hybrid structures were fabricated using multistep electron-beam lithography and thermal evaporation⁵⁰. Heater patterns were formed with aluminium and their sizes (D) were varied systematically over a wide size range, from 30 nm to 100 μm , in a periodic array with periodicity $L = 2D$. The thermally insulated hybrid region, separated from the heaters, is a bilayer structure consisting of a bottom layer of poly(methyl methacrylate), which has a low thermal diffusivity of $1.1 \times 10^{-7} \text{ m}^2 \text{ s}^{-1}$, and a top layer of silver, which has a lower thermoreflectance change than that of the heater. The detected thermoreflectance change signal has contributions from the geometry of the heaters, the surface temperature change and the thermoreflectivity.

Thermal and optical modelling. Multilayer thermal and optical transport simulations were carried out using a multilayer thermal model and Comsol Multiphysics (v4.3a). In the heat transfer module, periodic heat input and boundary conditions are applied, following the experimental conditions (see Supplementary Information). In the radiofrequency module, a linear temperature-dependence relative permittivity was considered, according to the measurement conditions. Three-dimensional thermoreflectance simulations were used to optimize the sample structure design and to ensure that the detected thermoreflectance signal could be determined by changes to the surface temperature of the heaters (for example, with more than 90% confidence in the sub-wavelength regime).

Variance reduced Monte Carlo simulation. The frequency-dependent phonon Boltzmann transport equation was solved using the recently developed variance reduced Monte Carlo method⁴¹ to model the quasi-ballistic phonon transport in the spectroscopy experiments. The simulation domain consists of periodic metallic dots

sitting on top of the underlying substrate materials, mimicking the experimental nanostructures. The phonon lifetimes calculated from first-principles DFT were used as the input properties for the simulation^{23,24}. The simulation was initialized by randomly populating a large number of computational phonon particles in the metal domain. Periodic boundary conditions were implemented to account for the periodicity of the entire simulation domain. At the end of each time step, the phonon energy was sampled in each discretized subcell and the local energy density was subsequently inverted to determine the local temperature distribution and the pseudo-temperature distribution. Anharmonic scattering was modelled as a probabilistic process following the energy sampling step. The surface temperature of the metal dots was recorded as a function of time and matched with the solution of Fourier's diffusion theory to obtain the effective thermal conductivity of the substrate.

Calculations to reconstruct the spectral distribution $\Phi(\lambda)$ from the size dependence $k(D)$. To obtain the suppression function $S(\chi)$ for the three-dimensional heating geometry, silicon was used as the benchmark reference material. Silicon has been well studied, and both experimental results for $k(D)$ (from this work) and theoretical data for $\Phi(\lambda)$ (ref. 23) are available for the full phonon spectrum. To numerically solve for $S(\chi)$ and the spectral distribution $\Phi(\lambda)$, we used a Gaussian quadrature with 50 points to discretize the integral in equation (1) and to obtain a singular linear system of equations that cannot be inverted using traditional methods. We instead used convex optimization^{51,52} to calculate $S(\chi)$ and recover $\Phi(\lambda)$, making use of the fact that both $S(\chi)$ and $\Phi(\lambda)$ are generally smooth functions that monotonically increase from 0 to 1. Our analysis does not make any assumptions regarding the phonon scattering mechanisms. More details about the convex optimization method and the numerical calculation for the one-dimensional case can be found in refs 43 and 51. To use convex optimization to solve for $S(\chi)$ and $\Phi(\lambda)$, we used CVX, a package for specifying and solving convex programs⁵².

References

- Hu, Y., Kuemmeth, F., Lieber, C. M. & Marcus, C. M. Hole spin relaxation in Ge-Si core-shell nanowire qubits. *Nature Nanotech.* **7**, 47–50 (2012).
- Grant, M. & Boyd, S. in *Recent Advances in Learning and Control* (eds Blondel, V., Boyd, S. & Kimura, H.) (Lecture Notes in Control and Information Sciences, Springer-Verlag, 2008).
- Grant, M. & Boyd, S. *CVX: Matlab software for disciplined convex programming, version 2.0 beta* (CVX Research, 2013); available at <http://cvxr.com/cvx>